

Geophysical Research Letters

RESEARCH LETTER

10.1029/2019GL084248

Key Points:

- Recent high-level observation campaigns provided data for the structure of the pressure maps to the upper levels of hurricanes
- These data show the existence of high-pressure regions in agreement with the hydrostatic summation of the near surface low and the warm core
- A clear violation of the gradient wind balance (nonbalance) is found around these highs

Correspondence to:

Y. Cohen,
yairchn@caltech.edu

Citation:

Cohen, Y., Durden, S. L., Harnik, N., & Heifetz, E. (2019). Relating Observations of Gradient Nonbalance at the Top of Hurricanes With Their Warm Core Structures. *Geophysical Research Letters*, 46, 11,510–11,519. <https://doi.org/10.1029/2019GL084248>



Received 23 JUN 2019

Accepted 12 SEP 2019

Accepted article online 21 OCT 2019

Published online 28 OCT 2019

Relating Observations of Gradient Nonbalance at the Top of Hurricanes With Their Warm Core Structures

Yair Cohen¹ , Stephen L. Durden², Nili Harnik³ , and Eyal Heifetz³

¹Geological and Planetary Sciences, California Institute of Technology, Pasadena, CA, USA, ²Jet Propulsion Laboratory, California Institute of Technology, Pasadena, CA, USA, ³Department of Geophysics, Porter School of the Environmental and Earth Sciences, Tel Aviv University, Tel Aviv, Israel

Abstract Recent analysis of Weather Research and Forecasting simulations shows that the flow around high-pressure regions that often develop at the top of Hurricanes (15-km altitude) violates the gradient wind balance, hence termed as “gradient nonbalance.” While observations at such high altitudes are rare, recently, NASA-HS3 and the Office of Naval Research-Tropical Cyclone Intensity campaigns deployed dropsondes from unprecedented levels around 18 km. In this work we use a wavenumber decomposition method to reproduce 2-D slices and 3-D structures from three storms from these campaigns: Edouard (2014), Joaquin (2015), and Patricia (2015). The analyzed data show that the development of high pressure at the hurricane’s top leads to various degrees of gradient nonbalance. These highs are a hydrostatic reflection of the storm tilt, which offsets the warm core with respect to the near surface low and the slanted eyewall. The implications of these findings and the relations with recent reports of upper-level wind field are discussed.

1. Introduction

Hurricanes are characterized by a low-level pressure anomaly of order 100 hPa (surface low) and a midlevel temperature anomaly of 10 K (warm core) with respect to their horizontal mean. The structure and position of the warm core with respect to the near surface low vary significantly in time and between storms (Stern & Nolan, 2012). The warm core is predicted to be wider than the near surface low, due to angular momentum conservation of the rising air that flares outward as it rises (Emanuel, 1986; Montgomery & Smith, 2014). Furthermore, the warm core is often observed to be offset from the position of the near surface low due to vertical wind shear (Creasey & Elsberry, 2017; Thomsen et al., 2015) precession or latitudinal changes in the Coriolis force.

The amplitude of the warm core (i.e., of the vertically integrated temperature anomaly) is known to be highly correlated with the minimum surface pressure in both models (Stern & Nolan, 2012) and observations (Doyle et al., 2017). However, the relationships between hurricane intensity and other aspects of the warm core structure, that is, its position, height, width, and the number of temperature peaks, are still debated. Some studies showed that the detailed structure of the warm core is related to the hurricane intensity in both models (Chen & Zhang, 2013; Ohno & Satoh, 2015) and observations (Halverson et al., 2006; Durden, 2013). However, other studies have argued against such a connection (Stern & Nolan, 2012; Stern & Zhang, 2013), invoking the hydrostatic balance to show that it is only the integrated effect of the warm core, rather than its vertical structure, that determines the surface pressure.

Hydrostaticity can only link the vertically integrated warm core structure to the vertical distance between two pressure levels, but not to the structure or position of either of them. Only after using an additional assumption about the geopotential height of the pressure field at one of these levels, can the geopotential height of the other level be inferred from the temperature field using the hypsometric equation. Typically, it is assumed that at the top of the troposphere geopotential gradients are negligible (so called the level of insignificant dynamics, LID, see Hirschberg & Fritsch, 1993), and the geopotential height there is set to a typical value for the tropical atmosphere. Then, the integrated warm core structure can be projected downward to give the surface pressure. Note that using these assumptions the warm core has exactly the same position and structure of the surface low from which it was projected. This stands in contrast to our understanding of hurricane structure in which the warm core is expected to be wider and is often offset from the near surface low. Moreover, observational evidence showing high-pressure anomalies at the upper levels

(Koteswaram, 1967) and tropopause doming (Duran & Molinari, 2018; Halverson et al., 2006) indicate that the upper-level pressure map is not necessarily gradient free. At the scale of a hurricane, high-pressure anomalies with an amplitude comparable to only 5-m/s geostrophic winds are sufficient to violate the gradient wind balance (Cohen et al., 2017, C17 hereafter).

It is, however, possible to reverse the downward projection of the temperature field as described above, by considering the surface pressure map as given only by the net overhead divergence, following Steenburgh and Holton (1993). Thus, given a near-surface pressure map, the warm core can be projected upward to obtain the hydrostatic structure of the upper-level pressure field. C17 showed that even slight differences in the position and structure of the warm core are enough for the hydrostatic summation to result in an upper-level pressure map with highly curved isobars that violated the gradient wind balance. In the absence of balance, part of the pressure gradient should act on the divergent component of the flow similar to the imbalance that exists due to friction near the surface. C17 showed that this nonbalance is often found in hurricanes simulated with the Weather Research and Forecasting model and correlates with some measures of intensity. Nonbalance was found to occur at levels of nearly 15 km, well above the typical flight level for dropsonde deployment.

Recently, two observation campaigns, The National Space and Aeronautic Administration's Hurricane and Severe Storm Sentinel (HS3), in its final year, and the Office of Naval Research's Tropical Cyclone Intensity (TCI), deployed dropsondes above 15 km. Specifically, the TCI campaign provided an exceptionally high horizontal resolution data set (up to 4 km) for the outflow level and the tropopause in hurricanes; see Doyle et al. (2017) and Duran and Molinari (2018).

In this work data from the HS3 and TCI are analyzed in light of the findings of C17 to examine if, and under what conditions, high-pressure regions develop at the top of observed hurricanes, how they are related to the warm core structures, and whether the flow around these high-pressure regions are expected to violate gradient wind balance. For this purpose, we produce both 2-D vertical slices and 3-D structure of these storms; the latter analysis is done using the wavenumber decomposition method outlined in Soukup and Marks (2017).

2. Nonbalance and Its Diagnosis

Gradient nonbalance (C17) is a scenario in which the gradient wind balance has no physical (mathematically real) solutions for a given pressure map. It is by definition a characteristic of the pressure map, *and not a characteristic of the flow itself*. Thus, nonbalance does not imply (cannot be inferred from) a cyclonic or anticyclonic flow. Nonbalance takes place only around a high, when the sum of the outward pointing centrifugal and pressure gradient forces cannot be balanced by the inward pointing Coriolis force. The diagnosis of nonbalance is presented here in both axisymmetric (for reference) and asymmetric (used in the study) coordinates.

In axisymmetric coordinates the radial momentum equation is written as follows:

$$\frac{\partial u}{\partial t} + u \frac{\partial u}{\partial r} + \omega \frac{\partial u}{\partial p} = \frac{v^2}{r} + fv - \frac{\partial \phi}{\partial r} \quad (1)$$

Here $r(u)$ is the radial coordinate (velocity), v the tangential velocity, and ω is the vertical velocity in pressure coordinates; ϕ is the geopotential of a pressure surface p , and f is the Coriolis parameter (assumed here as constant).

A nonvanishing right-hand side (RHS) of equation (1), defined as gradient nonbalance, implies radial acceleration and a condition of nonbalance is given by $Ro_g = v_g/fr < -1/4$, where v_g is the geostrophic wind in the axisymmetric system (see C17).

In an asymmetric case, such as shown in Figure 2 in C17, high-pressure anomalies of noncircular shapes that are located off the storm center might develop. The centrifugal forces acting on air parcels in balanced flow around such high pressure depend on the local curvature of the isobars rather than on the radial distance from these storm centers. Accordingly, nonbalance can be defined based on the local curvature of the isobars by using natural coordinates, for example, Chapter 4 in Holton (2004). In natural coordinates, the downwind and cross wind components (respectively) of Newton's second Law are as follows:

$$\hat{s} : \frac{\partial V}{\partial t} + V \frac{\partial V}{\partial s} + \omega \frac{\partial V}{\partial p} = - \frac{\partial \phi}{\partial s} \quad (2)$$

$$\hat{n} : \frac{V^2}{R} + fV = - \frac{\partial \phi}{\partial n} \quad (3)$$

Here \hat{s} and \hat{n} are the unit vectors in the downwind and cross wind directions, respectively, with \hat{n} positive when pointing to the left. R is the local radius of curvature of the trajectory, defined as positive (negative) around cyclonic (anticyclonic) flow. V is the positive-definite amplitude of the wind vector $\vec{V} = \hat{s}V$. It is important to notice that equation (3) does not imply that gradient balance holds, as part of the pressure gradient resides on the RHS of equation (2). For balance to hold, each of the sides in equation (2) must vanish independently.

The approach for identifying nonbalance follows an indirect path. By assuming that gradient wind balance does hold, the RHS term in equation (3) is the total pressure gradient and may be expressed as fV_g , here V_g is the geostrophic wind amplitude. Moreover, under the assumption of balance, the wind follows the isobars, and thus, R is calculated from the curvature of the isobars. Dividing equation (3) by f^2R yields

$$Ro^2 + Ro = Ro_g \quad (4)$$

Here $Ro = V/fR$ is the Rossby number, $Ro_g = V_g/fR$ is the geostrophic Rossby number. Equation (4) classifies the possible solutions of the gradient balance and has nonphysical (complex) solutions for $Ro_g < -1/4$ (see Cohen et al., 2015; C17). Since Ro_g is proportional to $1/R$, the size of a high at the upper level is related to the size of the storm; thus smaller storms are more likely to produce nonbalance.

The main challenge in diagnosing Ro_g locally is the calculation of the curvature radius $R(x,y)$. Previous works calculated the radius of curvature of the flow from the downwind change in \hat{s} , see equations (14, 15) in Alaka (1961). In the current study, however, we are interested in calculating the curvature radius of the isobars irrespective of the wind trajectory. This can be done by noting that the 2-D curl of a vector field in natural coordinates is the sum of the shear and the curvature:

$$\vec{\nabla} \times \vec{A} = \hat{k} \left(\frac{\partial A}{\partial n} + \frac{A}{R} \right) \quad (5)$$

where \hat{k} is the vertical unit vector. Thus, if \vec{A} is taken as a unit vector parallel to the isobars at every point, the shear vanishes and one obtains:

$$\vec{\nabla} \times \left(\frac{-\hat{k} \times \vec{\nabla} \phi}{\|\vec{\nabla} \phi\|} \right) = \frac{\hat{k}}{R} \quad (6)$$

This amounts to decomposing the gradient of 2-D geopotential data at each pressure level to its two horizontal components, rotating each of the components by $\pi/2$, normalizing them by the magnitude of the total gradient, and taking the 2-D curl of the rotated normalized components.

In the analysis we limit the value of the curvature radius to more than 20 km in order to prevent small scale, instantaneous features from dominating the signal (the observed nonbalance prevails even if this threshold is 100 km).

This curvature radius calculation allows us to analyze balance and nonbalance regions of the asymmetric pressure map at the top of hurricanes.

3. Data and Analysis

Data for this research are taken from the 2014 period of the HS3 (Braun et al., 2016) and from the TCI (Doyle et al., 2017). In both campaigns dropsondes were deployed from the WB-57f aircraft at about 18 km providing direct measurements at the level of interest for nonbalance.

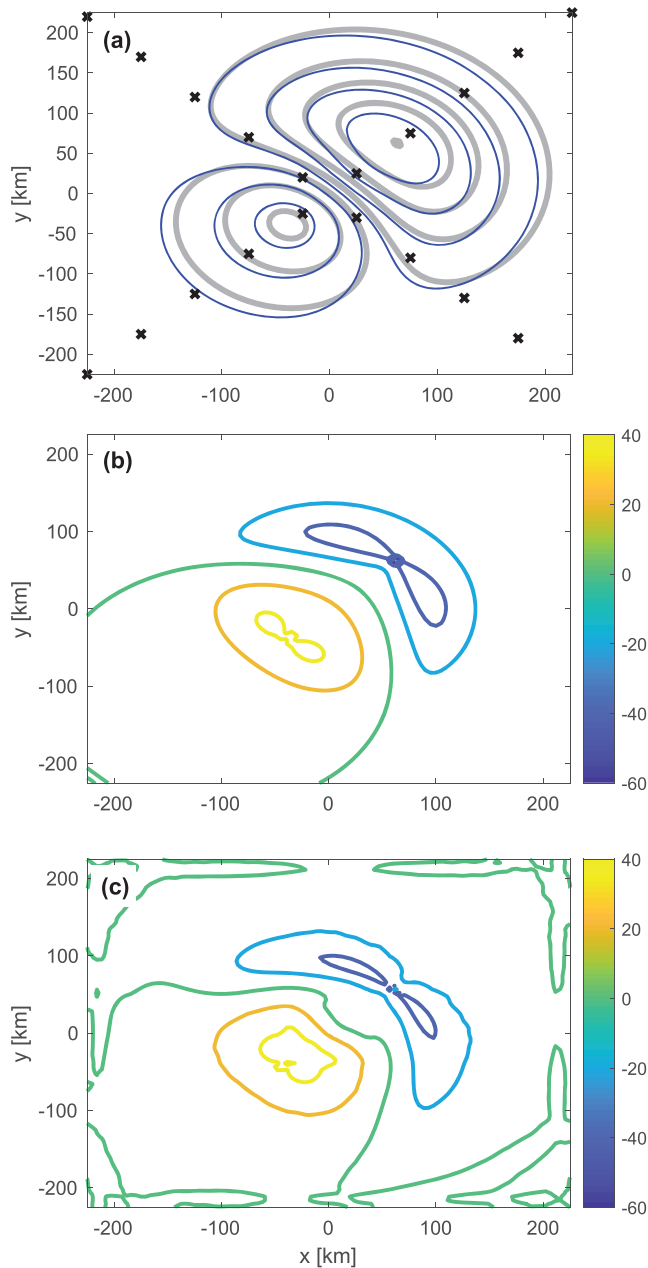


Figure 1. A test of the wavenumber decomposition method in reconstructing asymmetric geopotential field and its gradient based Ro_g calculation from dropsonde-like subsampling. (a) Original dummy geopotential field (gray), subsampling points in black x markers and the reconstructed field in blue contours. (b) The Ro_g field of the original (gray) geopotential field at the top. (c) The Ro_g calculated from the reconstructed field.

Three storms are analyzed: Edouard (2014) from HS3 and Joaquin (2015) and Patricia (2015) from TCI. These storms were chosen since they are the best sampled and prominent (most intense and developed). The specific days in these storms were chosen since in these days the flight path was crossing the storm center at least twice, allowing for a composition of the 3-D structure from the figure-four flight path. In TCI (Patricia and Joaquin) the dropsonde spacing is 20–50 km in the outer region and less than 10 km in the inner core (see Doyle et al., 2017), while in HS3 (Edouard) dropsonde spacing is order of magnitude larger. The time between the first and last dropsonde is about 6 hr.

Dropsonde data include the simultaneous measurements of the latitude, longitude, and height coordinates, the three wind components, and the pressure and the temperature. The horizontal position and horizontal velocities were converted to storm relative coordinates with the position of the storm center taken from the Hurricane Research Division: https://www.aoml.noaa.gov/hrd/data_sub/hurr.html and linearly interpolated to the relevant times. In rare cases we find unrealistic values at a point along the profiles, and in such cases we interpolate between neighboring points to replace the bad data. The “clean” data were interpolated along the pressure coordinates to fixed 10-hPa intervals and analyzed in two manners: First, we produce vertical cross sections of the storm along the flight path to examine the location of the warm core with respect to the storm center. Second, we estimate the 3-D structure of the storm using a wavenumber decomposition method at each vertical level, following Soukup and Marks (2017), described here in short:

Let $D(\lambda, \varphi)$ represent a set of data points sampled from a “figure-four” flight in each latitude and longitude (λ, φ , respectively). The data D are projected to polar coordinates about the center of the storm $D(r, \theta)$ and interpolated to a radial grid of 10-km resolution. At each radial point r_i a third-order polynomial of the angular coordinate, $F(\theta)$, is fitted to the four azimuthal data points available $D(r_i, \theta_j)$. In order to force the angular periodicity of the fitted function we include the first (last) data point of $F(\theta)$ again in a $+2\pi$ (-2π) phase from its original position. The product of cosine (sine) functions with the fitted polynomial function $F(\theta)$ is then numerically integrated to obtain the coefficients of the sine (S) and cosine (C) components of the data for wavenumbers $j = 0, 1, 2$, and 3:

$$C_0(r) = \frac{1}{2\pi} \int_0^{2\pi} F(\theta) d\theta \quad (7)$$

$$C_j(r) = \frac{1}{\pi} \int_0^{2\pi} F(\theta) \cos(j\theta) d\theta \quad (8)$$

$$S_j(r) = \frac{1}{\pi} \int_0^{2\pi} F(\theta) \sin(j\theta) d\theta \quad (9)$$

with $S_0 = 0$. The interpolated data $d(r, \theta)$ is computed as follows:

$$d(r, \theta) = \sum_{j=0}^3 C_j(r) \cos(\theta_j) + S_j(r) \sin(\theta_j) \quad (10)$$

The convergence of the interpolated field shown in Soukup and Marks (2017) allows to approximate the true field using only Wavenumbers 0 through 3, given that the center of interpolation is close enough to the center of the storm in lower levels.

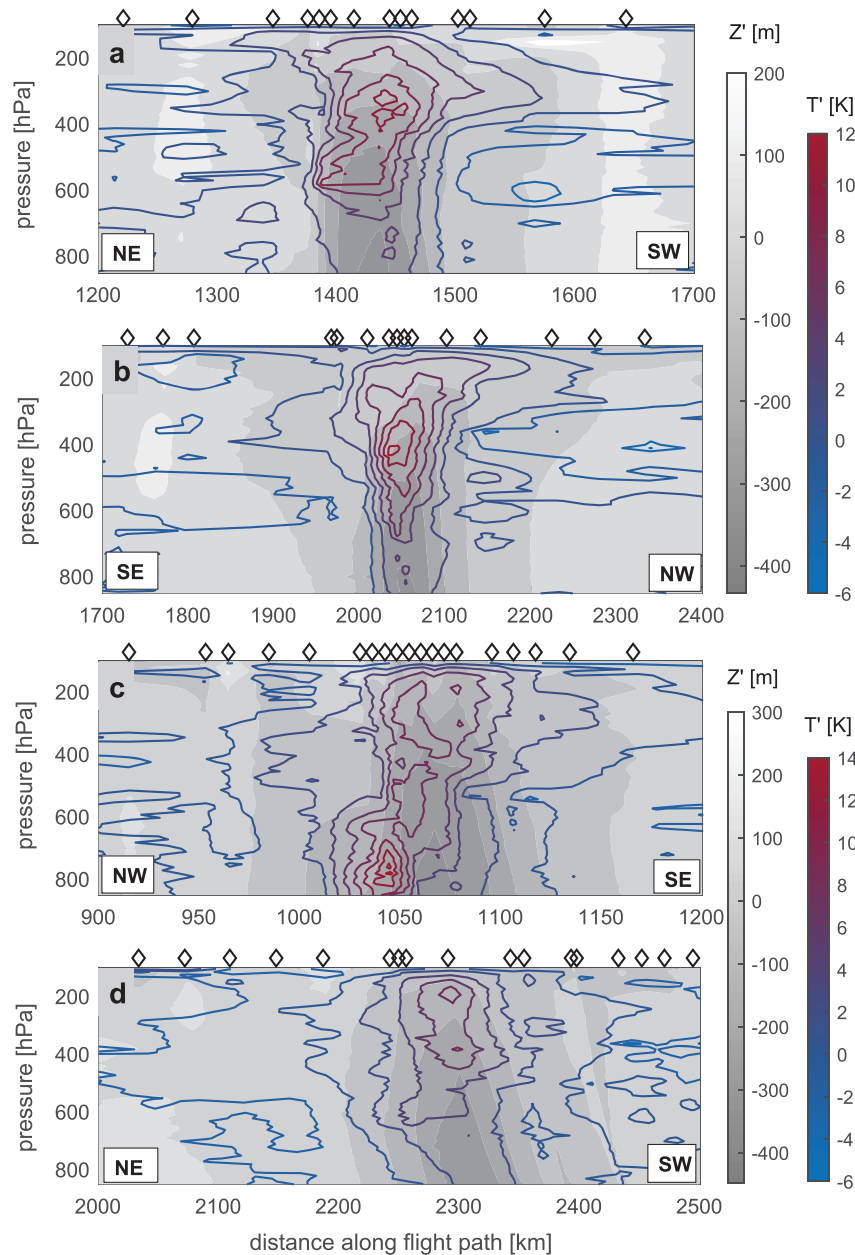


Figure 2. Vertical cross sections along the Tropical Cyclone Intensity flight transects of Joaquin (2015) in two consecutive days: panels (a), northeast to southwest, and (b), southeast to northwest for 2 October 2015 and panels (c), northwest to southeast, and (d), northeast to southwest, for 3 October 2015. Gray shading shows geopotential height anomaly, Z' (m), color contours shows temperature anomaly with respect to the horizontal mean, T' (K), and black diamonds indicate the deployment location of dropsondes.

A simple test for the ability of this method is demonstrated in Figure 1a where gray contours show a hypothetical asymmetric geopotential map, based on C17. This map is subsampled (at 50-km spacing) along a hypothetical figure-four “flight” path (black x markers) and a wavenumber decomposition is applied in order to approximate the original geopotential field (blue contours). The interpolated geopotential field captures essential features of the original map, that is, a small high next to a wider low, and generally underestimates the absolute values of Ro_g . This method was tested for both northeast and east warm core deflection and performed with similar quality for dropsonde spacing of up to ~ 200 km (not shown). Moreover, as the interpolation center differs from the storm center, both the 850 and 150 hPa deteriorate at equal rate (not shown). Thus, we judge the validity of our interpolation of observations by inspecting circular shape of the 850 hPa.

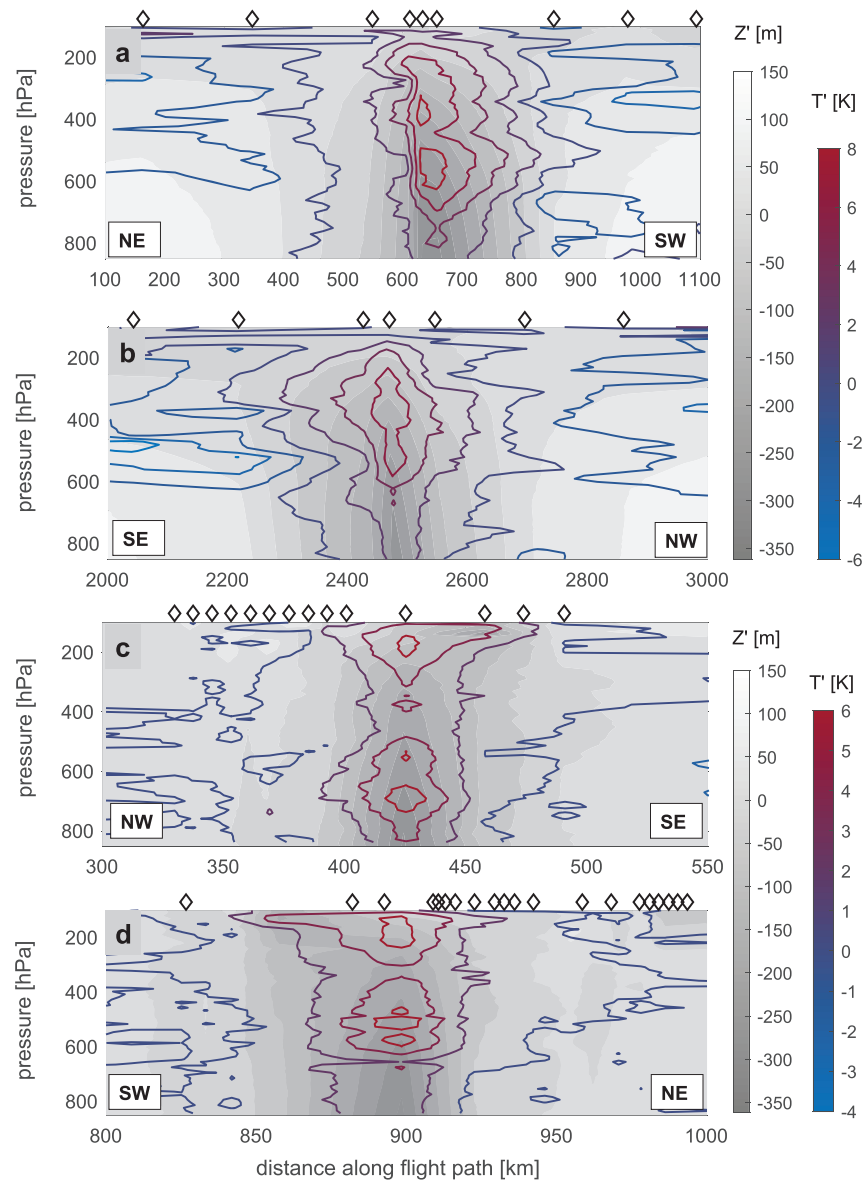


Figure 3. Similar to Figure 2 but for the HS3 flight transects of Edouard 2014 on 16 September (a and b) and for the Tropical Cyclone Intensity flight transects of Patricia 2015 on 22 October (c and d).

Figures 1b and 1c show the Ro_g field calculated from the original and interpolated data, respectively. The errors in interpolated Ro_g field are small compared to the signal and small compared to the values found in the observations in the next section.

4. Results

Figures 2a and 2b, and 2c and 2d show transects along the flight paths from Joaquin (2015) on 2 and 3 October, respectively. Storm's tilt reflected in the position of minimum geopotential with height is aligned with the upper-level warm core position (defined in all cases as temperature anomaly from the horizontal mean). On 2 October the Joaquin (2015) has an eastward tilt with the warm core anomaly concentrated mostly in the upper levels (as the 2-K anomaly contour), a maximum wind of 56 m/s and the minimum pressure of 941 hPa. On 3 October Joaquin (2015) has a northward tilt with the secondary warm core anomaly developing at the lower levels. Thus, the warm core itself is tilted from northwest around the 700 hPa

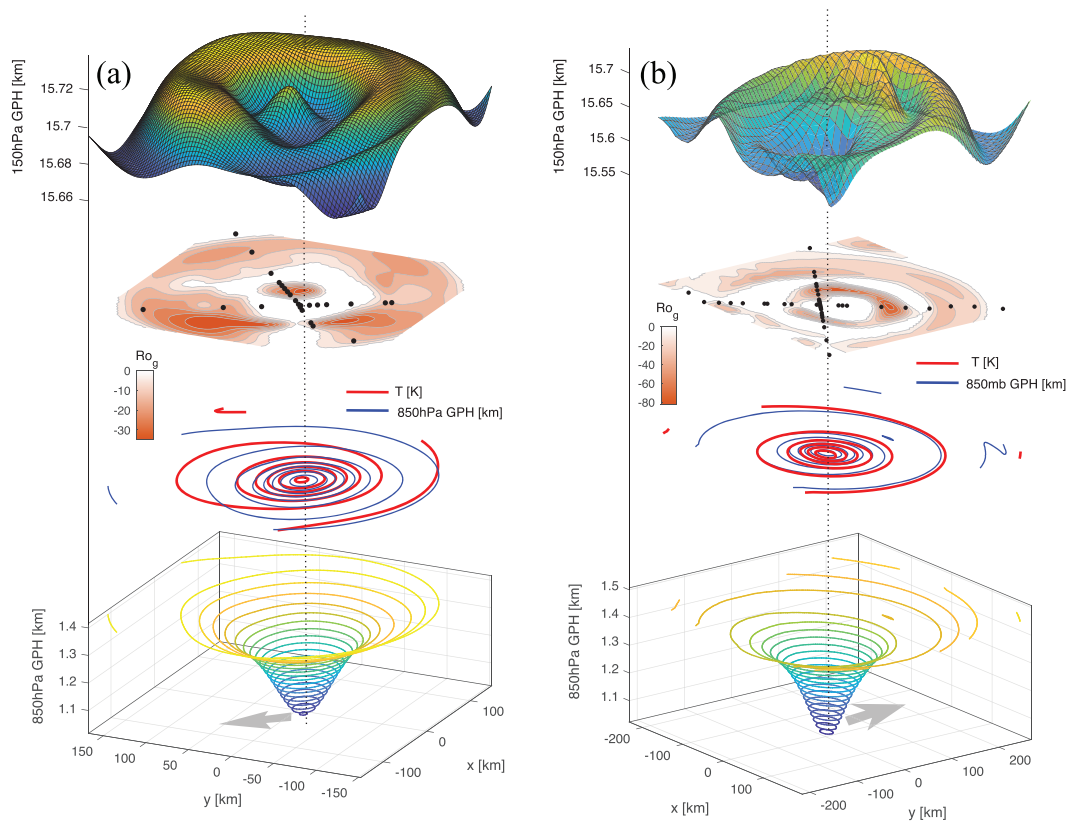


Figure 4. A visualization of the 3-D storm structure using selected horizontal slices to illustrate relevant features. Each panel shows from bottom to top: 3-D contours of the 850-hPa geopotential height (km); the overlap of the 850 hPa (blue) and the vertically mean temperature (red); shaded contours of Ro_g evaluated on the 150h-Pa surfaces (only negative values are shown) along with the deployment position of the dropsondes used; surface map of the 150-hPa geopotential height (km). The 3-D structure is obtained using the wavenumber decomposition of dropsonde data. (a) The approximated structure of Joaquin (2015) on 2 October and (b) the approximated structure of Joaquin (2015) 3 October. Gray arrows at the bottom indicate the approximate direction of storm tilt.

southeast around the 250-hPa level (see the southeast to northwest transect in panel c). The storm's maximum wind is 70 m/s, and the minimum pressure is 934 hPa. (We note that Creasey & Elsberry, 2017, found significant storm tilt in Joaquin [2015], on 4 October in their analysis of TCI data).

Figures 3a and 3b show transects from Edouard (2014) on 16 September showing eastward tilt with a double peak warm core structure. Figures 3c and 3d show transects from Patricia (2015) on 22 October (with maximum wind of 61 m/s) with almost no tilt and a warm core with at least three prominent peaks, where the upper warm core anomaly is tilted southward.

Using the wavenumber decomposition, Figures 4 and 5 show a 3-D depiction of the structure of these storms on these specific days with a clearly hydrostatic picture. The relative position of the temperature anomaly dominated by the warm core (red contours) with respect to the near surface low (blue contours) is shown in the second axes. The imprint of hypsometric sum of these fields is evident in the shape of the 150-hPa surface at the top, even though the latter is calculated from the observed data directly.

On 2 October, Joaquin (2015) has a strong, northwest, warm core tilt and a wider warm core that is reflected in the shape of the 150-hPa level with a large wide annulus shaped high pressure. On 3 October, Joaquin (2015) has a much more moderate, northward, warm core tilt that is visible in the crescent shape high at the 150 hPa. In both days the Ro_g values are far from balance with higher peak values on 3 October but with a larger region of nonbalance on 2 October. We note that the maximum wind on 3 October is higher, yet we cannot causally link the two. On 16 September Edouard shows a strong northeast tilt of the warm core and a corresponding high-pressure anomaly to the northeast at the 150-hPa level (Figure 5a). Patricia (2015) on 22 October (at the peak of its intensification, see Rodgers et al., 2017; Duran & Molinari, 2018) shows an almost perfect vertical alignment and almost perfect axisymmetric structure (Figure 5b). A slight

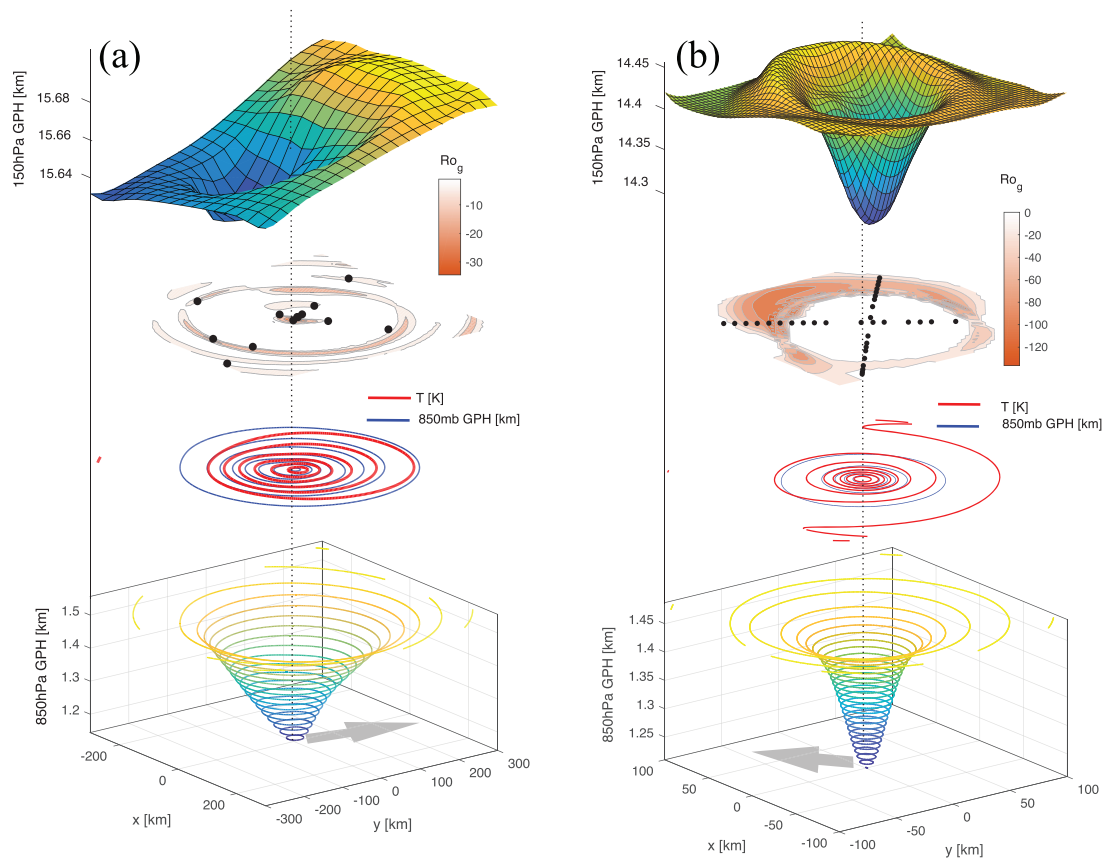


Figure 5. Similar to Figure 4 but for the structure of Edouard (2014) on 16 September (a) and Patricia (2015) on 22 October (b).

northwest tilt of the warm core is evident with a corresponding asymmetry of the 150-hPa map. The annulus shape on that day shows the hydrostatic signature of a warm core that is wider than the near surface low, as predicted theoretically (Eliassen, 1951; Emanuel, 1986).

5. Discussion

In all cases considered here we find significant nonbalance. Upon examining the value of geopotential gradient and radius of curvature that compose these Ro_g values, we find that a significant part of the nonbalance results from the strong pressure gradients developing in the annulus shaped high. For instance, in the case of Patricia (2015) shown in Figure 5b we find $\nabla\phi = -0.015 \text{ m/s}^2$ (corresponding with $|V_g| = 400 \text{ m/s}$) in regions of $Ro_g = -100$. Thus, even though some peak values of negative Ro_g might be regarded as an artifact of unrealistically small curvatures, the bulk of the nonbalance cannot be dismissed.

The amount of nonbalance found in Edouard (2014) is notably smaller than that found in Patricia (2015) and Joaquin (2105). This could be a result of low dropsonde resolution, yet it is important to notice that Edouard (2014) is a much larger storm with radius of maximum wind nearly four times that of Patricia (2015) and Joaquin (2105). The $1/r$ dependence of Ro_g implies that larger storms, like Edouard (2014), are less likely to generate significant nonbalance as it would require much sharper negative pressure gradients at its upper levels.

The flight transects in Figures 2 and 3 clearly show that the warm core in observed storms is both wider and offset with respect to the near surface low. These differences between the warm core and surface low stand in contrast to the hydrostatic relation between the two as is assumed in the standard balanced vortex model. However, the well-known and robust relationship between warm core temperature and minimum surface pressure is indisputable in full physics models and observations. Thus, it seems that this relation is a

reflection of a much more complicated dynamics in which the net overhead divergence and convergence in the column amount to a surface pressure that correlates with the warm core anomaly.

The momentum equations imply that the excess of the pressure gradient and the centrifugal force that cannot be balanced by the Coriolis force should accelerate the cross isobaric (i.e., divergent) flow. The wind speed sampling of the dropsondes does not provide a very reliable set for a wavenumber decomposition of the 3-D wind field. Even at the 850 hPa where we have a clearer expectation of what the structure of the wind field should be, we could not obtain a reliable wind field from the wavenumber decomposition. Thus, we cannot accompany our upper pressure map with a reliable upper-level wind field. However, since 2016 a new Solid State Tail Doppler Radar has become operational in measurements of wind speeds up to the 16-km level. Measurements in Hurricane Michael (2018) P. Reasor, private communication, showed a maximum of divergent outflow at 15 km with wind amplitudes at the distance of radius of maximum wind, that are not far from that found in lower levels, see HRD (2018a), yet with a much larger divergent component than in lower levels, see HRD (2018b). Unfortunately, such radar observations are not available for the same hurricanes in which high-level dropsondes were deployed and it is thus difficult to examine whether the nonbalance part of the pressure gradient is collocated with the divergent component of the winds. It is our hope that our findings, together with other recent findings such as the dramatic tropopause height changes reported in Duran and Molinari (2018), will motivate a combined upper-level dropsondes and new Solid State Tail Doppler Radar campaign in the future.

Acknowledgments

Y. Cohen acknowledges Paul Reasor from HRD for providing the analysis of the SS-TDR showing upper-level winds. Part of this work was performed by the Jet Propulsion Laboratory, California Institute of Technology under contract with the National Aeronautics and Space Administration. The comments of two anonymous reviewers have greatly improved the presentation of the ideas developed in this study. The dropsonde data used in this study are available online: for the TCI campaign (https://www.eol.ucar.edu/field_projects/tci) and for the HS3 (https://www.nasa.gov/mission_pages/hurricanes/missions/hs3/).

References

- Alaka, M. A. (1961). The occurrence of anomalous winds and their significance. *Monthly Weather Review*, *88*, 482–494.
- Braun, S. A., Newman, P. A., & Heymsfield, G. M. (2016). NASA's hurricane and severe storm sentinel (HS3) investigation. *Bulletin of the American Meteorological Society*, *97*(11), 2085–2102. <https://doi.org/10.1175/BAMS-D-15-00186.1>
- Chen, H., & Zhang, D. L. (2013). On the rapid intensification of Hurricane Wilma (2005). Part II: Convective bursts and the upper-level warm core. *Journal of the Atmospheric Sciences*, *70*(1), 146–162. <https://doi.org/10.1175/JAS-D-12-062.1>
- Cohen, Y., Dvorkin, Y., & Paldor, N. (2015). Linear instability of warm core, constant potential vorticity, eddies in a two-layer ocean. *Quarterly Journal of the Royal Meteorological Society*, *141*(690), 1884–1893. <https://doi.org/10.1002/qj.2493>
- Cohen, Y., Harnik, N., Heifetz, E., Nolan, D. S., Tao, D., & Zhang, F. (2017). On the violation of gradient wind balance at the top of tropical cyclones. *Geophysical Research Letters*, *44*, 8017–8026. <https://doi.org/10.1002/2017GL074552>
- Creasey, R. L., & Elsberry, R. L. (2017). Tropical cyclone center positions from sequences of HDSS sondes deployed along high-altitude overpasses. *Weather and Forecasting*, *32*(1), 317–325. <https://doi.org/10.1175/WAF-D-16-0096.1>
- Doyle, J. D., Moskaitis, J. R., Feldmeier, J. W., Ferek, R. J., Beaubien, M., Bell, M. M., et al. (2017). A view of tropical cyclones from above: The tropical cyclone intensity experiment. *Bulletin of the American Meteorological Society*, *98*(10), 2113–2134. <https://doi.org/10.1175/BAMS-D-16-0055.1>
- Duran, P., & Molinari, J. (2018). Dramatic inner-core tropopause variability during the rapid intensification of hurricane Patricia (2015). *Monthly Weather Review*, *146*(1), 119–134. <https://doi.org/10.1175/MWR-D-17-0218.1>
- Durden, S. L. (2013). Observed tropical cyclone eye thermal anomaly profiles extending above 300 hPa. *Monthly Weather Review*, *141*(12), 4256–4268. <https://doi.org/10.1175/MWR-D-13-00021.1>
- Eliassen, A. (1951). Slow thermally or frictionally controlled meridional circulation in a circular vortex. *Astrophysica Norvegica*, *5*, 19.
- Emanuel, K. A. (1986). An air-sea interaction theory for tropical cyclones. Part I: Steady-state maintenance. *Journal of the Atmospheric Sciences*, *43*(6), 585–605. [https://doi.org/10.1175/1520-0469\(1986\)043<0585:AASITF>2.0.CO;2](https://doi.org/10.1175/1520-0469(1986)043<0585:AASITF>2.0.CO;2)
- Halverson, J. B., Simpson, J., Heymsfield, G., Pierce, H., Hock, T., & Ritchie, L. (2006). Warm core structure of hurricane Erin diagnosed from high altitude dropsondes during CAMEX-4. *Journal of the Atmospheric Sciences*, *63*(1), 309–324. <https://doi.org/10.1175/JAS3596.1>
- Hirschberg, P. A., & Fritsch, J. M. (1993). On understanding height tendency. *Monthly Weather Review*, *121*(9), 2646–2661. [https://doi.org/10.1175/1520-0493\(1993\)121<2646:OUHT>2.0.CO;2](https://doi.org/10.1175/1520-0493(1993)121<2646:OUHT>2.0.CO;2)
- Holton, J. R. (2004). *An introduction to dynamic meteorology* (4th ed.). Burlington, MA: Elsevier Academic Press.
- HRD. (2018a). Plan view of wind vectors in Michael (2018). Retrieved 2018-10-10, from ftp://ftp.aoml.noaa.gov/hrd/pub/data/RTradar/20181010H1/181010H1_ws_dbz_upper_planview.png
- HRD. (2018b). Vertical section of wind amplitude in Michael (2018). Retrieved 2018-10-10, from ftp://ftp.aoml.noaa.gov/hrd/pub/data/RTradar/20181010H1/181010H1_0949_ws_profile.png
- Koteswaram, P. (1967). On the structure of hurricanes in the upper troposphere and lower stratosphere. *Monthly Weather Review*, *95*(8), 541–564. [https://doi.org/10.1175/1520-0493\(1967\)095<0541:OTSOHI>2.3.CO;2](https://doi.org/10.1175/1520-0493(1967)095<0541:OTSOHI>2.3.CO;2)
- Montgomery, M. T., & Smith, R. K. (2014). Paradigms for tropical cyclone intensification. *Australian Meteorological and Oceanographic Journal*, *64*(1), 37–66. <https://doi.org/10.22499/2.6401.005>
- Ohno, T., & Satoh, M. (2015). On the warm core of a tropical cyclone formed near the tropopause. *Journal of the Atmospheric Sciences*, *72*(2), 551–571. <https://doi.org/10.1175/JAS-D-14-0078.1>
- Rodgers, R., Aberson, S., Cecil, D., Doyle, J., Morgerman, J., Kimberlain, T., et al. (2017). Re-writing the tropical record books: The extraordinary intensification of Hurricane Patricia (2015). *Bulletin of the American Meteorological Society*, *98*(10), 2091–2112. <https://doi.org/10.1175/BAMS-D-16-0039.1>
- Soukup, G. A., & Marks, F. D. (2017). Evaluation of hurricane wind speed analyses in a simulation of hurricane Earl (2010) using low-order wavenumbers. *Monthly Weather Review*, *145*(8), 3223–3245. <https://doi.org/10.1175/MWR-D-14-00281.1>
- Steenburgh, W. J., & Holton, J. R. (1993). On the interpretation of geopotential height tendency equations. *Monthly Weather Review*, *121*(9), 2642–2645. [https://doi.org/10.1175/1520-0493\(1993\)121<2642:OTIOGH>2.0.CO;2](https://doi.org/10.1175/1520-0493(1993)121<2642:OTIOGH>2.0.CO;2)

- Stern, D. P., & Nolan, D. S. (2012). On the height of the warm core in tropical cyclones. *Journal of the Atmospheric Sciences*, 69(5), 1657–1680. <https://doi.org/10.1175/JAS-D-11-010.1>
- Stern, D. P., & Zhang, F. (2013). How does the eye warm? Part I: A potential temperature budget analysis of an idealized tropical cyclone. *Journal of the Atmospheric Sciences*, 70(1), 73–90. <https://doi.org/10.1175/JAS-D-11-0329.1>
- Thomsen, G. L., Smith, R. K., & Montgomery, M. T. (2015). Tropical cyclone flow asymmetries induced by a uniform flow revisited. *Journal of Advances in Modeling Earth Systems*, 7, 1265–1284. <https://doi.org/10.1002/2015MS000477>